New physics searches with an optical dump at LUXE

Zhaoyu Bai,[1,2,*] Thomas Blackburn,[3,†] Oleksandr Borysov,[4,‡] Oz Davidi,[2,§] Anthony Hartin,[5,‖] Beate Heinemann,[4,6,¶] Teng Ma,[7,**] Gilad Perez,[2,††] Arka Santra,[2,‡‡] Yotam Soreq,[7,§§] and Noam Tal Hod[2,‖‖]

[1]*Department of Physics, Southern University of Science and Technology, Shenzhen 518055, China*
[2]*Department of Particle Physics and Astrophysics, Weizmann Institute of Science, Rehovot 7610001, Israel*
[3]*Department of Physics, University of Gothenburg, SE-41296 Gothenburg, Sweden*
[4]*Deutsches Elektronen-Synchrotron DESY, 22607 Hamburg, Germany*
[5]*University College London, Gower Street, London WC1E 6BT, United Kingdom*
[6]*Albert-Ludwigs-Universität Freiburg, 79104 Freiburg, Germany*
[7]*Physics Department, Technion—Israel Institute of Technology, Haifa 3200003, Israel*

(Received 14 October 2021; revised 26 June 2022; accepted 3 December 2022; published 28 December 2022)

We propose a novel way to search for feebly interacting massive particles, exploiting two properties of systems involving collisions between high energy electrons and intense laser pulses. The first property is that the electron-laser collision results in a large flux of hard photons, as the laser behaves effectively as a thick medium. The second property is that the emitted photons free-stream inside the laser and thus for them the laser behaves effectively as a very thin medium. Combining these two features implies that the electron-intense-laser collision is an apparatus, which can efficiently convert $\mathcal{O}(10\ \mathrm{GeV})$ electrons to a large flux of hard, collinear photons. The photons are directed onto a solid dump in which feebly interacting massive particles may be produced. With the much smaller backgrounds induced by the photon beam compared to those expected in electron- or proton-beam dump experiments and combined with a relatively shorter dump used here, the sensitivity to short lifetimes is unparalleled. We denote this novel apparatus as "optical dump" or NPOD (new physics search with optical dump). The proposed LUXE experiment at the European XFEL has all the basic required ingredients to realize this experimental concept for the first time. Moreover, the NPOD extension of LUXE is essentially parasitic to the main experiment and thus, practically it does not have any bearing on its main program. We discuss how the NPOD concept can be realized in practice by adding a detector after the last physical dump of the experiment to reconstruct the two-photon decay of a new spin-0 particle. We show that even with a relatively short dump, the search can still be background-free. Remarkably, even with a few days of data taking with a 40 TW laser corresponding to its initial run, LUXE-NPOD will be able to probe an uncharted territory of models with pseudoscalars and scalars. Furthermore, with a 350 TW laser of the main run, LUXE-NPOD will have a unique reach for these models. In particular it can probe natural scalar theories for masses above 100 MeV. We note that the new NPOD concept may be ported to other existing or future facilities worldwide, including, e.g., future lepton colliders.

DOI: 10.1103/PhysRevD.106.115034

*zhaoyu.bai@weizmann.ac.il
†tom.blackburn@physics.gu.se
‡oleksandr.borysov@desy.de
§oz.davidi@weizmann.ac.il
‖anthony.hartin@desy.de
¶beate.heinemann@desy.de
**t.ma@campus.technion.ac.il
††gilad.perez@weizmann.ac.il
‡‡arka.santra@weizmann.ac.il
§§soreqy@physics.technion.ac.il
‖‖noam.hod@weizmann.ac.il

I. INTRODUCTION

Despite its great success, the standard model (SM) of particle physics does not provide a complete description of Nature; new particles and/or forces are required to account for the observed neutrino oscillations, dark matter, and the cosmological baryon asymmetry. This provides us with a strong motivation to search for new physics (NP), yet the above observations cannot be robustly linked to a specific microscopic physical scale. Therefore, there are worldwide efforts to probe physics beyond the SM (BSM) at different energy scales in different types of experimental frontiers, see, e.g., Ref. [1] for a recent discussion. Despite all of these efforts we are currently lacking a "smoking gun" for a direct observation of NP. This calls for new experimental

approaches that may open the window to alternative ways to search for BSM physics.

In this work, we introduce a novel way to search for feebly interacting particles (FIPs), using collision of high energy electrons with intense laser pulses. Our proposal highlights the complementary between the largely unexplored nonperturbative and nonlinear quantum electrodynamics (QED) phenomena, such as Schwinger pair production in a strong electromagnetic (EM) field [2–4], and the quest for BSM physics. We point out that an intense laser behaves as a new type of a particularly-effective dump for the incoming electron beam as follows. In the collision between a high-energy electron beam and an intense laser, the laser behaves as a thick medium, leading to the production of a large flux of hard photons [5–9]. Furthermore, as the photons have a negligible interaction with the EM field, they practically free stream in the laser after being produced, see Fig. 1. Thus, the outgoing photon flux can be used to search for weakly interacting new particles that couple to photons, covering an uncharted territory of the relevant parameter space, see Fig. 5.

Let us comment about the essential advantage of this proposal compared with other state-of-the-art beam-dump based setups. In other experiments, photons may be produced by placing a thin solid target to induce bremsstrahlung processes. However, in that case the photons are generated from weakly-coupled processes, and consequently, the flux per-electron obtained with such a design is more than an order of magnitude lower than what can be achieved with the nonlinear NPOD idea. Alternatively, the new particles can be produced from secondary photons that are produced when an electron (or proton) beam is directly shot on a thick solid target.

The main advantage of the NPOD idea is that the corresponding background can be significantly [$\mathcal{O}(100)$] lower compared to conventional beam dump experiments mentioned above, while the signal yield in the latter is only a factor of few larger. To explain that intuitively, let us focus on a fixed initial beam of N_e electrons with $\mathcal{O}(10\text{–}20)$ GeV each. In the NPOD case, one will typically generate $\sim 2N_e$ photons (above 1 GeV) that will reach the dump for the NP production there. In the other case, there will be instead $\sim 9N_e$ photons (above 1 GeV), all produced after (but close to) the beginning of the dump. While having more photons available for new physics production, this case also features a significantly increased hadronic and electromagnetic activity in the dump.

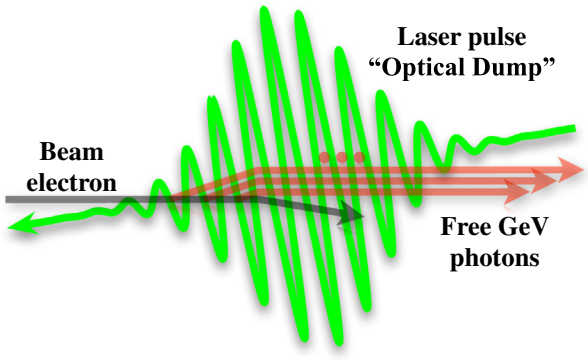

FIG. 1. Schematic illustration of the optical dump. The high intensity laser pulse behaves effectively as a thick medium for the incoming electron, that in turn may emit a large flux of hard photons which "free stream" in this optical medium and can be used to search for new physics.

Consequently, the number of particles escaping the dump will be larger by a factor of $\mathcal{O}(10)$, which is roughly the ratio between the incoming electron energy and the typical energy of the photons in the NPOD case. Since the analysis requires two photons per signal candidate, and since the background mostly consists of photons and neutrons faking photons in the detector, the two-photon background is ultimately $\mathcal{O}(> 10^2)$ larger than in the NPOD case (assuming the same initial beam, the same solid target and the same detector). These advantages are not inherent for LUXE and hence they make the new NPOD concept applicable in a variety of existing/future facilities worldwide.

Concretely below, we focus below on the proposed LUXE experiment [10,11] at the Eu.XFEL [12]. We demonstrate that it has the potential to probe an unexplored, well motivated, parameter space of new spin-0 (scalar or pseudoscalar) particles with coupling to photons. This proposal is denoted as LUXE-NPOD: *New Physics at Optical Dump*. LUXE is planning to start with a 40 TW laser (phase-0) and later deploy a 350 TW laser (phase-1). This setup can probe spin-0 particles with masses up to $\mathcal{O}(350)$ MeV and a decay constant of $\mathcal{O}(10^5\text{–}10^6)$ GeV, beyond the reach of existing limits.

II. ELECTRON-LASER COLLISIONS

The interaction between high-energy electrons and intense laser pulses is reviewed in [5,6,13–15]. Here we highlight the relevant points required for the LUXE-NPOD proposal, where the electron's energy is $\approx$16.5 GeV and there are $\sim 10^9$ of them per bunch crossing (BX). The behavior of an electron traveling inside an intense laser pulse can be described by treating the laser as a background field. The modified electron-field modes are known as Volkov states [16], denoted as e^-_V below. These states provide an exact solution to the corresponding modified Dirac equation. Emission processes and pair production are then evaluated using perturbation theory, the "Furry picture" [17], similar to what is done in the background-free case. In contrast, the photons can be described as background-free fields, similar to free photons propagating in space.

The passage of an electron inside the laser pulse is controlled by two processes related to each other by an exchange of the initial and final states. The first process is the

Compton scattering [18,19] (often referred as high-intensity or nonlinear Compton scattering), $e^-_V \to e^-_V + \gamma$, where our focus is on cases where, in the lab frame, the electron emits a photon, γ, at $\mathcal{O}$(few) GeV. The typical timescale for this process is $\tau_\gamma = 1/\Gamma_\gamma \sim \mathcal{O}(10)$ fs. The second process to be discussed below, is the Breit-Wheeler pair production [20] (often referred as one photon pair production or nonlinear Breit-Wheeler pair production), $\gamma \to e^+_V + e^-_V$. In practice, this process can be viewed as if the original electron first emits a photon, which subsequently interacts with the laser leading to the production of a pair of Volkov states. The typical pair production timescale relevant to LUXE is $\tau_{ee} = 1/\Gamma_{ee} \sim \mathcal{O}(10^4$–$10^6)$ fs [11]. The typical laser pulse duration foreseen at LUXE is $t_L \sim \mathcal{O}$(10–200) fs, and finally, the relevant time scale of LUXE's 800 nm laser itself is $\sim 1/\omega_L \sim$ 0.4 fs [11], where ω_L is the laser angular frequency.

We find the following hierarchy among these four timescales to be $1/\omega_L \ll \tau_\gamma \lesssim t_L \ll \tau_{ee}$. Several points are in order as follows: (i) the fact that $1/\omega_L$ is the shortest scale in the problem supports the treatment of the laser as a background field (along with the large occupation number of the laser photons) to a leading order; (ii) the fact that τ_{ee} is much longer than all the other scales in the problem implies that we can treat the photons in the laser as free streaming; and (iii) the fact that τ_γ is shorter than t_L implies that it behaves as a thick target for the electrons. For an ideal large pulse (spatially and temporally), the electrons will in principle lose all their energy to the photons. The combination of points (ii) and (iii) above and the resulting hard spectrum of photons is the core reason for why we denote our experiment as optical dump and for being a novel concept to search for FIPs.

In practice, due to the limited size and duration of the laser's pulse [11], the beam electrons at LUXE are not stopped. These electrons are deflected away by a magnet right after the interaction with the laser. The region after the electron-laser interaction chamber in Fig. 3 can be considered as being effectively free from any electrons that passed the optical dump region.

To contrast the optical dump with a conventional solid-dump, consider the propagation of high energy electron or photon in the dump. In both cases the mean free path is controlled by scattering of the highly charged heavy nucleus, which is of the order of the electron radiation length, X_0 (see, e.g., Ref. [21]). This is an important difference between the laser medium and a solid-material medium. In the former, the pulse length can be made long compared to the photon production timescale, while being short enough compared to the pair production one, i.e., $\tau_\gamma \lesssim t_L \ll \tau_{ee}$. Therefore, a few hard photons (with $E_\gamma \gtrsim$ 1 GeV on average) per incoming electron exit the laser pulse. In the thick limit of a solid-material dump, if the material length, d, is much larger than X_0, all of the hard photons will be absorbed in the material. In the thin solid-material limit, where $d \ll X_0$, the hard bremsstrahlung photons can escape the material, but their production rate is suppressed by $d/X_0 \ll 1$. For example, in phase-1 of LUXE (or with a thin solid-material with $d/X_0 \sim 0.1$) we expect $\gtrsim$1.7 (or ∼0.06) photons with $E_\gamma > 1$ GeV per incoming electron.

Another important feature of the NPOD idea in the context of LUXE, is that it can be viewed as a parasitic extension, i.e., it does not drive the design and operation of the main experiment. In principle, this may be compared with a simpler experiment, where the same initial electron beam is shot directly on the same dump. This hypothetical setup is denoted hereafter as e-dump. As we argued above, while the NPOD case can be background-free, the background in the e-dump case will be excessive. Nevertheless, we provide a quantitative study of this setup below. Furthermore, unlike LUXE-NPOD, the e-dump setup is by-construction dedicated experiment. The e-dump hypothetical setup should therefore be regarded only as a reference in the comparisons given below.

The resulting (primary and secondary) photons spectra for LUXE-NPOD case are shown in Fig. 2. The thin solid-material case and the e-dump case are also shown for reference.

III. NEW PHYSICS SCENARIOS

We consider new spin-0 particles, which are found in well motivated extensions of the SM. We focus on two cases: a pseudo-scalar, a, which is often called axionlike particle (ALP), and a scalar, ϕ. Light ALPs arise in variety of models motivated by the Goldstone theorem, with their

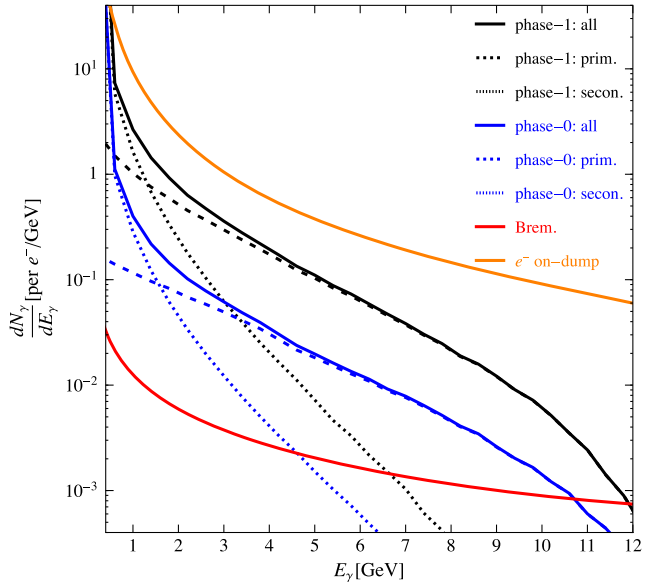

FIG. 2. The emitted photon spectrum for LUXE-NPOD phase-0 (1) in blue (black) compared to the perturbative bremsstrahlung spectrum with $E_e = 16.5$ GeV and target length of $0.01X_0$ in red and to photons from the electron beam shot on the same dump (the e-dump setup) in orange.

masses protected by a shift symmetry, see Refs. [22–26] for recent reviews. In addition, we consider a *CP* even, ϕ, where theoretically, constructing a natural model of a light scalar is rather challenging. However, two concrete proposals have been put forward, one where the scalar mass is protected by an approximate scale-invariance symmetry (see for instance [27] and Refs. therein), and a second one where it is protected by an approximate shift-symmetry that is broken, together with *CP* [28,29], by two sequestered sectors (inspired by the relaxion paradigm [30]). For simplicity, we study *CP* conserving model (either ALP or scalar) described by a single coupling to photons and captured by

$$\mathcal{L}_{a,\phi} = \frac{a}{4\Lambda_a} F_{\mu\nu}\tilde{F}^{\mu\nu} + \frac{\phi}{4\Lambda_\phi} F_{\mu\nu}F^{\mu\nu}, \tag{1}$$

where $F_{\mu\nu}$ is the photon field strength and $\tilde{F}_{\mu\nu} = \frac{1}{2}\epsilon_{\mu\nu\alpha\beta}F^{\alpha\beta}$. The decay rate of the ALP into two photons are given by $\Gamma_{a\to 2\gamma} = m_a^3/(64\pi\Lambda_a^2)$ (for scalar replace a with ϕ).

The ϕ-photons coupling induces, quadratically divergent, additive contribution to the scalar mass-square, $\delta m_\phi^2 \sim \Lambda_{\rm UV}^4/(16\pi^2\Lambda_\phi^2)$. This leads to a naturalness bound $\Lambda_\phi \gtrsim 4\times 10^5\ \text{GeV}(\frac{\Lambda_{\rm UV}}{\text{TeV}})^2 \frac{200\ \text{MeV}}{m_\phi}$, where $\Lambda_{\rm UV}$ is the scale in which NP is required to appear in order to cancel the quadratic divergences. Moreover, the same loop diagram as above induces a mixing between the Higgs and the ϕ scalar. This mixing can be estimated by calculating the square mixed mass term $\delta\mu_{H\phi}^2 \sim \Lambda_{\rm UV}^4\alpha/(64\pi^3\Lambda_\phi v)$, where $v \simeq 246$ GeV is the Higgs VEV. Thus, the $H-\phi$ mixing is $\theta_{H\phi} \sim 10^{-6}(\frac{\Lambda_{\rm UV}}{\text{TeV}})^4 \frac{4\times 10^5\ \text{GeV}}{\Lambda_\phi}$, which is in an unconstrained region of parameter space of Higgs portal (or relaxion) models. See Refs. [1,31] for a recent analysis.

We mainly focus on processes involving ALP and scalar production, which are equal in the coherent production limit (used here), we therefore denote them simply as $X = a, \phi$. The photons produced in the electron-laser collisions (see Fig. 2 for the spectra) are freely propagating to collide with the nuclei, N, of the material of some sizable dump to produce NP. Thus, the X are produced via Primakoff like production, $\gamma + N \to N + X$. An illustration of this process is provided in Fig. 3 (top) in the context of LUXE along with the associated background topologies (bottom). Another mechanism is *Primary NP production*, where the NP is directly produced at the electron-laser interaction region via X electron coupling, see Appendix B for further details.

IV. THE LUXE-NPOD PROPOSAL

We propose to use the high flux of GeV photons, emitted from LUXE's electron-laser interaction region, to search for FIPs of spin-0. We present the experimental setup and assume a given flux of hard photons. After being produced, the photons freely propagate to a physical dump and interact with its nuclei to produce the X particle.

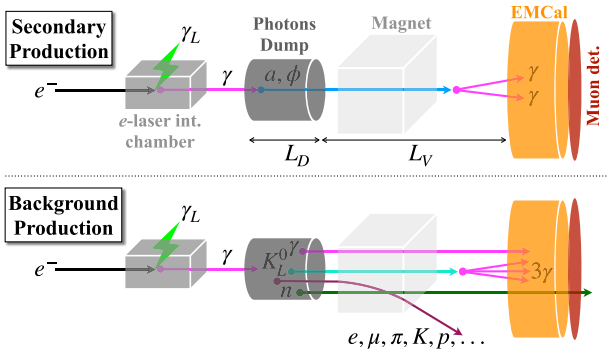

FIG. 3. A schematic illustration of the LUXE-NPOD concept. Top: the secondary production mechanism realization in the experimental setup. Bottom: the relevant background topologies. The electrons are deflected by a magnet placed right after the interaction chamber.

The dump is of length L_D and it is positioned ∼13 m away from the electron-laser interaction region. The X particles are long-lived and hence, they will travel some distance before decaying into $\gamma\gamma$. Therefore, an empty volume of length L_V is left at the back of the dump to allow the X particles to decay back into two photons. The two-photon signature is our signal in the detector which is positioned at L_V after the dump.

The expected number of X's produced and detected in the proposed setup shown in Fig. 3 (top) can be approximated as (see, e.g., Refs. [32,33]),

$$N_X \approx \mathcal{L}_{\rm eff} \int dE_\gamma \frac{dN_\gamma}{dE_\gamma}\sigma_X \left(e^{-\frac{L_D}{L_X}} - e^{-\frac{L_V+L_D}{L_X}}\right)\mathcal{A}, \tag{2}$$

with $\sigma_X \propto Z^2$ is the Primakoff cross section, e.g., [34,35], Z is the nuclear charge, $\mathcal{L}_{\rm eff}$ is the effective luminosity discussed below, E_γ is the incoming photon energy, $L_X \equiv c\tau_X p_X/m_X$ is the propagation length of the X particle, with τ_X and $p_X \approx \sqrt{E_\gamma^2 - m_X^2}$ being its proper life-time and momentum, respectively. $\mathcal{A}$ stands for the angular acceptance and efficiency of the detector.

We estimate N_X independently by using a MADGRAPH5 v2.8.1 [36–39] Monte Carlo simulation, including an event-by-event acceptance estimation. We use the UFO model [39] from Ref. [40] and follow Refs. [33,41,42] for the form factors. The results of the approximation in Eq. (2) and the MADGRAPH5 simulation are found to be in a very good agreement.

As a benchmark, we consider a tungsten (W) dump with $L_D = 1.0$ m and a radius of 50 cm. With this choice, the effective or integrated luminosity can be written as $\mathcal{L}_{\rm eff} = N_e N_{\rm BX}\frac{9\rho_W X_0}{7A_W m_0}$ [41], where ρ_W is the W density, A_W is its mass number and X_0 is its radiation length (all taken from [21]). $N_e N_{\rm BX}$ is the experiment repetition. The remaining

parameter is the nucleon mass, $m_0 = 1.66 \times 10^{-24}$ g. An electron beam with a bunch population of $N_e = 1.5 \times 10^9$ electrons is assumed with a fixed energy of $E_e = 16.5\,\mathrm{GeV}$, and the outgoing photon spectrum from the electron-laser interaction is denoted as dN_γ/dE_γ. These are typical Eu.XFEL operation parameters as discussed in [11]. We further assume one year of data taking, corresponds to 10^7 live seconds of the experiments. Thus, $N_{\mathrm{BX}} = 10^7$ laser-pulse and electron-bunch collisions (or BXs) for a laser with a 1 Hz repetition rate.

For the detector, we assume a disk-like structure with a radius of $R = 1$ m positioned at $L_V = 2.5$ m after the end of the dump and concentric with it. We assume a minimal photon-energy threshold of 0.5 GeV for detection and hence, a signal event is initially identified as having two photons in the detector surface with $E_\gamma > 0.5$ GeV. In addition, we show that two final photons can be effectively separated, see Appendix D.

The differential photon flux per initial electron, dN_γ/dE_γ shown in Fig. 2, includes photons from the electron-laser interaction, as well as secondary photons produced in the EM shower which develops in the dump. With $L_D \gtrsim 0.2$ m, all of the primary photons are stopped in the dump.

The primary photon flux is determined from full strong-field QED Monte Carlo simulation [43], using probability rates derived in [44] and corresponding to the two LUXE benchmarks (phase-0 and phase-1) which mostly differ by the laser power (40 TW and 350 TW respectively). This simulation code has been benchmarked extensively against theoretical calculations from strong-field QED [45]. Based on an initial optimization, trying to maximize the flux of photons with energies above 1 GeV (see Fig. 95 in [11]), a laser pulse length of 25(120) fs for phase-0 (1) with a transverse spot-size of 6.5(10) μm (full width at half maximum) is assumed. These pulse configurations correspond to an intensity parameter of $\xi \simeq 3.2(3.4)$ for phase-0 (1). The laser intensity parameter is $\xi \equiv e\mathcal{E}/(m_e\omega_{\mathrm{L}})$ where $\mathcal{E}$ is magnitude of the laser's electric field and $\omega_{\mathrm{L}} \sim 1.5$ eV is the energy of the laser photon (at 800 nm wavelength). These parameters are already sufficient to demonstrate the capability of the NPOD proposal: further optimization of the electron-laser collision will be considered in future work. For a dump at a distance of 13 m from the interaction point, about 95% of the emitted photons fall inside a radius of 5 cm. The photon passage through the dump material and the evolution of the shower inside the dump are simulated with GEANT4 v 10.06.p01 [46–48] (using the QGSP_BERT physics list). Since the emitted Compton photon flux was never measured at the laser parameters of LUXE, we propose to use the measured flux in order to normalize N_a in-situ, i.e., taking dN_γ/dE_γ from the experimental measurement planned at LUXE. The measurements of both the flux and the value of ξ will be available per BX by several independent detectors of the main experiment [11].

A tungsten dump of $L_D = 1.0$ m is effectively blocking all incident primary Compton photons. However, the SM particles produced in the dump during the shower generate backgrounds of three types: (i) charged particles, namely electrons, muons and hadrons; (ii) fake photons: mostly neutrons misidentified as photons; and (iii) real photons: mostly from EM/hadronic interactions close to the end of the dump, or from meson decays in the volume.

These backgrounds rates are estimated using a detailed GEANT4 simulation as discussed below. Our simulation includes a detailed description of only the beam, the dump (with its supporting structure) and a conceptual detector, i.e., we do not attempt to simulate the response of a specific detector technology. All particles that reach this conceptual detector surface are recorded in terms of their position, momentum, origin and time-of-arrival. We consider a minimum threshold of 0.5 GeV per photon.

Although incorporating a specific implementation of a real detector in the simulation is beyond the scope of this work, we argue that with current detector technologies this search can be regarded as background-free. The main aspects of a realistic detector that are crucial to suppress the background completely are good angular and energy resolution to allow the reconstruction of the decay point and the mass of the hypothetical X particle. Additionally, timing resolution can be used to efficiently reject photons produced via secondary neutron interactions. In the discussion below, we quantify the overall impact of these requirements on the rejection and further assume that a detector fulfilling the minimum set of these requirements can be built.

While the background levels for phase-0 are softer and smaller than those of phase-1, the same levels are conservatively assumed hereafter also for phase-0.

V. BACKGROUNDS DISCUSSION

The rate of charged SM particles (mostly muons and protons), which in principle arrive at the detector with a minimum energy of 0.5 GeV, is smaller by roughly a factor of 10 compared to the rate of neutrons with the same characteristics (the neutrons are also typically more energetic). These and other charged particles can be effectively bent away from the detector surface by a magnetic field of $B \approx 1$ T over an active bending length of $\sim$1 m. Furthermore, muons from the dump or from cosmic rays, which do arrive at the detector can be vetoed with dedicated muon-chambers placed behind and above the photon detector. Hence, the charged particle component is not considered as background in the following discussion.

Thus, focusing on background photons and/or neutrons, we denote the average number of particles with energy above 0.5 GeV arriving at the conceptual detector surface per one BX as $\mu_x(L_D)$. In this notation, x is a neutron ($x = n$) or a photon ($x = \gamma$) and L_D is measured in meters. The sources for both background photons and neutrons are

dominated by the hadronic activity close to the end of the dump, with photons mostly originating from meson decay near the dump-edge. This is further discussed in Appendix C. We note that the background photons yield includes both prompt photons from the dump as well as all kinds of decays of SM particles, as illustrated in Fig. 3.

Following a GEANT4 run with 10^{10} primary photons (equivalent to ~2 BXs), which are distributed according to the photon spectrum of LUXE's phase-1 from Fig. 2, we find that the number of such neutrons per BX is $\mu_n(1.0\text{ m}) = 10 \pm 2.3$, where the error is statistical only. In the same run, we also find zero photons and thus, we can only infer from it that $\mu_\gamma(1.0) < 3$. A statistically precise estimation of $\mu_\gamma(1.0\text{ m})$ is rather challenging computationally, since the number of BXs simulated has to be a few orders of magnitude larger than what is simulated now.

We approach the problem of extracting $\mu_\gamma(1.0\text{ m})$ in two independent analyses that yield consistent results. Both approaches are based on the modeling of the amount of particles that exit the dump as a function of its length. This modeling is achieved by fitting the results from repeated simulation runs for different L_D values below its nominal value to allow for adequate background photon statistics. For $L_D < 1$ m, both $\mu_\gamma(L_D)$ and $\mu_n(L_D)$ become large enough such that our statistical error becomes sufficiently small and we can confidently fit the model's parameters. In our first approach we simply model the exiting photon flux as an exponentially falling distribution of L_D, while in the second approach we assume that the photon to neutron number ratio is constant with L_D. Both approaches yield a consistent result as expected, but we focus below on the second approach since it gives a slightly larger estimate of the background and hence, a more conservative projection.

In the second approach, the extrapolation to the nominal case of $L_D = 1.0$ m is done by fitting the ratio $R_{\gamma/n} = \mu_\gamma(L_D)/\mu_n(L_D)$ vs $L_D < 1.0$ m to a zeroth order polynomial and multiplying the result by the number of neutrons per BX obtained for the nominal case of $L_D = 1.0$ m, i.e., $\mu_\gamma(1.0\text{ m}) \approx \mu_n(1.0\text{ m}) \times R_{\gamma/n}$. The result of the fit for five such runs starting from $L_D = 0.30$ m and going up to $L_D = 0.50$ m in steps of 0.05 m is $R_{\gamma/n} = 0.0013 \pm 0.0002$. The reduced χ^2 of the fit is 1.88. The data and fit can be seen in Fig. 4, which validates the assumption of approximately constant ratio. In the absence of data around $L_D \approx 1$ m, the flat ratio assumption is essentially the simplest one can make, which also provides a capping to the extrapolated background. Different assumptions for the modeling of the ratio were tested as well, but were found to yield slightly lower levels of backgrounds and hence, we remain with the flat ratio assumption for the subsequent analysis.

Figure 4 also shows the same ratio for the hypothetical e-dump setup and otherwise the same conditions as discussed above. The only difference is that instead of simulating 10^{10} primary photons, we simulate 3×10^9 monochromatic ($E_e = 16.5$ GeV) primary electrons. The spectrum of the photons produced in the resulting shower inside the dump is also shown in Fig. 2. The fit result for the hypothetical e-dump case is $R_{\gamma/n} = 0.0062 \pm 0.0002$, i.e., significantly larger than for the LUXE-NPOD setup. This difference implies that while the two-photon background induced by real photos or neutrons faking photons may be manageable for the LUXE-NPOD setup with a reasonable assumption of a specific detector technology, it will be nonmanageable for the hypothetical e-dump setup for the same technology assumption (and moreover for a similar "protons on dump" case).

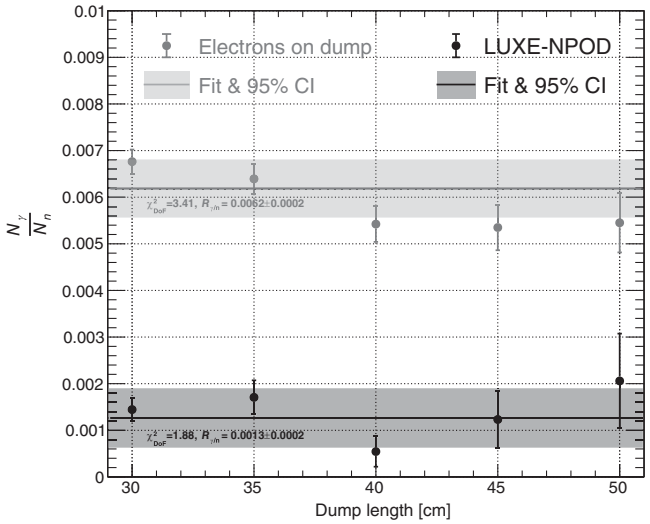

FIG. 4. The ratio of number of photons to the number of neutrons vs different dump lengths ranging from 30 cm to 50 cm for the LUXE-NPOD setup in black. For comparison, the same ratio is given for the hypothetical e-dump setup in gray. Each data point corresponds to a full simulation of two BXs for the given dump length. Beyond 50 cm, there are only a few or no photons left and hence these points are not simulated. The fits to a zeroth order polynomial of the ratios are shown along with the corresponding 95% confidence intervals. The fitted ratio, $R_{\gamma/n}$, is used to derive the probabilities to find two photons (real or fake) as discussed in the text.

The extrapolated number of photons per BX for the nominal case of $L_D = 1.0$ m is therefore $\mu_\gamma(1.0\text{ m}) = 0.013 \pm 0.004$. In the following discussion we will omit the dump length notation, while still assuming $L_D = 1.0$ m, i.e., $\mu_\gamma = \mu_\gamma(1.0\text{ m})$ and $\mu_n = \mu_n(1.0\text{ m})$.

The number of background events over some period of run-time, where two photons are detected in the same BX can be calculated from the probability to find two real photons or two fake photons (neutrons misidentified as photons) or one real photon and one fake photon per BX in the detector volume:

(i) the probability to find two real photons is $P_{2\gamma} = \mathcal{P}(\mu_\gamma, 2)$, where $\mathcal{P}$ is a Poisson probability,

(ii) the probability to find two fake photons from neutrons is $P_{2n\to 2\gamma} = \sum_{k_n=2}^{\infty} \mathcal{P}(\mu_n, k_n) \times \mathcal{B}(2, k_n, f_{n\to\gamma}) = f_{n\to\gamma}^2 e^{-\mu_n f_{n\to\gamma}} \mu_n^2/2$, where $\mathcal{B}$ is a binomial probability, k_n is the number of neutrons and $f_{n\to\gamma}$ is the probability to misidentify a neutron as a photon with $E_\gamma > 0.5$ GeV, and

(iii) the probability to find one real photon and one fake photon from a neutron is $P_{n+\gamma\to 2\gamma} = \mathcal{P}(\mu_\gamma, 1) \times \sum_{k_n=1}^{\infty} \mathcal{P}(\mu_n, k_n) \times \mathcal{B}(1, k_n, f_{n\to\gamma}) = (\mu_\gamma e^{-\mu_\gamma})(f_{n\to\gamma} e^{-\mu_n f_{n\to\gamma}} \mu_n)$.

For the values of μ_γ and μ_n obtained above, the resulting probabilities are $P_{2\gamma} \approx 8.3 \times 10^{-5}$, $P_{2n\to 2\gamma} \approx 50 f_{n\to\gamma}^2 e^{-10 f_{n\to\gamma}}$, and $P_{n+\gamma\to 2\gamma} \approx 0.13 f_{n\to\gamma} e^{-10 f_{n\to\gamma}}$, respectively. The "fake rate", $f_{n\to\gamma}$, depends strongly on the specific detector technology choice. The dump itself can be further optimized to maximize the effective luminosity and the signal production rate, while minimizing the hadronic interaction length, using a combination of materials, and an improved geometry. Besides minimizing $f_{n\to\gamma}$, the number of two-photon background events estimated from the probabilities above can be reduced by a set of selection requirements based on the reconstructed properties of the two-photon system. These may include, for example, requirements on the invariant mass, the common vertex, the X production vertex and the timing. As for $f_{n\to\gamma}$, the projected performance of these requirements depends strongly on the detector technology. The rejection power of the full selection criteria per BX is hereafter denoted as $R_{\rm sel}$. For simplicity, we assume that $R_{\rm sel}$ is similar between the different background components. The number of background two-photon events in one year (with $N_{\rm BX} = 10^7$) is estimated to be $N_{\rm b} = N_{\rm BX} P_{\rm b} R_{\rm sel}$, where $\mathrm{b} = 2\gamma, 2n \to 2\gamma$ and $n + \gamma \to 2\gamma$ for the three background components respectively. The numerical estimates for these three channels are therefore:

$$N_{2\gamma} \approx 8.3 \times 10^2 R_{\rm sel}, \tag{3}$$

$$N_{2n\to 2\gamma} \approx 5.0 \times 10^8 f_{n\to\gamma}^2 e^{-10 f_{n\to\gamma}} R_{\rm sel}, \tag{4}$$

$$N_{n+\gamma\to 2\gamma} \approx 1.3 \times 10^6 f_{n\to\gamma} e^{-10 f_{n\to\gamma}} R_{\rm sel}. \tag{5}$$

We see that with $R_{\rm sel} \leq 10^{-3} - 10^{-4}$ and $f_{n\to\gamma} \leq 10^{-3} - 10^{-4}$ we can achieve < 1 background events. Hence, our projections for the sensitivity assumes a background-free experiment. Consequently, the 95% C.L. region corresponds to $N_X = 3$.

The requirements on $R_{\rm sel}$ and $f_{n\to\gamma}$ can be translated to a general requirement for the detector performance. For $R_{\rm sel}$ the main properties that can be used to discriminate between signal and background are the azimuthal angles of the two photons, the decay vertex two photons, the transverse momentum of the two-photon system and the invariant mass. For neutron rejection in addition the calorimeter shower properties and the time of arrival can be explored. It can be shown that the required background reduction is achievable with existing detector (calorimeter) technologies: time resolution[1] of $\sim\mathcal{O}(10\text{–}100)$ ps [49–51], energy resolution of a few percent and finally, position and angular resolutions of $\sim\mathcal{O}(100)$ μm and $\sim\mathcal{O}(100)$ mrad respectively [49,51–53]. We note that even a subset of these specifications is sufficient to meet our minimal requirements for the search.

TABLE I. The two-photon background components (combination of real photons and/or fake photons from neutrons) and their sum for LUXE-NPOD, compared with the hypothetical case of e-dump.

Background component	LUXE-NPOD	e-dump
2γ	0.42	130
$n + \gamma \to 2\gamma$	0.32	21
$2n \to 2\gamma$	0.06	1
Total	∼0.8	∼150

For completeness, we also quote the values of μ_n and μ_γ resulting from a simulation of two BXs of e-dump case discussed above. These are found to be $\mu_n(1.0) = 42.6 \pm 4.6$ and $\mu_\gamma(1.0) = 0$. The derivation of the different background components is identical to the one given above for the LUXE-NPOD setup. Using $\mu_n(1.0)$ along with the average ratio of photon per neutron (see Fig. 4), we estimate that $\mu_\gamma(1.0) \approx 0.26$ for the e-dump setup, i.e., a factor of 20 larger than for LUXE-NPOD. Plugging in the numbers as shown above, the comparison between the background rates of LUXE-NPOD to e-dump for 10^7 BX's and assuming $R_{\rm sel} = 5 \times 10^{-4}$ and neutron to photon fake rate of $f_{n\to\gamma} = 5 \times 10^{-4}$ is given in Table I.

As one can see, the background in the case of e-dump is at least two orders of magnitude larger than in the case of LUXE-NPOD. Although the "protons on dump" case is not simulated for this study, it is expected to be even larger than the e-dump case. Hence, the X search becomes much more challenging in terms of the requirements on the detector and on the offline analysis if one is to start from the e-dump (or "protons on dump") case instead.

In addition, the background rate in LUXE-NPOD phase-0 will be much smaller. Thus, LUXE-NPOD can be still in a background-free region with much looser detector requirements. This is not the case for e-dump, where the backgrounds become much larger due to the worse detector. This can be demonstrated as follows. Let us assume a detector with $R_{\rm sel} = f_{n\to\gamma} = 5 \times 10^{-3}$. We can conservatively assume that the photons-to-neutrons ratio is similar to phase-1. However, the number of neutrons can be scaled down roughly by the ratio of the initial photon spectra

[1]The ultimate time resolution of the EM calorimeter will also determine the required cosmic muons veto strength and hence the required arrangement of muon chambers.

between phase-0 and phase-1 as $\sim 1/10$ (see Fig. 2). Thus, we have ~ 1 neutron per BX for a dump of 1 m, leading to 0.0013 photons per BX (instead of 0.013 in phase-1). The resulting total background budget for phase-0 with a looser detector requirements, compared with the e-dump setup, is estimated as ~ 0.95 and ~ 4000 for LUXE-NPOD and e-dump setups, respectively. This should be compared with the bottom row of Table I. The signal for e-dump is larger by factor of ~ 20 than for LUXE-NPOD in phase-0. However, while LUXE-NPOD may still remain background-free, even with loosened detector requirements (compared with those of phase-1), the background in the e-dump case with the same detector increases to an effectively unmanageable level.

The background estimations discussed above rely on the conservative assumption that for a fixed energy threshold, the ratio of the number of photons to the number of neutrons which arrive at the detector face per BX is approximately constant for different dump lengths, so that it can be extrapolated from short dumps. This assumption is important due to the extreme computational difficulty to fully simulate enough bunch crossings to allow a reliable estimation of the number of two-photon events with $E > 0.5$ GeV at $L_D = 1$ m. In that case, more than $\sim 10^7$ bunch crossings would be needed. We leave this extreme simulation campaign to a future work and instead, we rely on the flat ratio assumption.

VI. PROJECTED SENSITIVITY

In the reminder of the discussion, our projections for the sensitivity assume a background-free experiment. Consequently, the 95% C.L. region corresponds to $N_X = 3$.

The sensitivity projections of LUXE-NPOD for $N_X = 3$ are shown in Fig. 5 for the X mass versus the effective coupling as defined in Eq. (1). The contours for different N_X values are shown in Appendix A. We compare the result to the current bounds from LEP [54–56], PRIMEX [35,57], NA64 [58,59], Belle-II [60], and beam-dumps experiments [61,62]. In addition, the future projections of NA62 (in dump-mode), NA64, Belle-II, FASER, PRIMEX and GLUEX [35,63–67] are presented. We see that already in phase-0 LUXE can probe an unexplored parameter space in the mass range of 50 MeV $\lesssim m_X \lesssim$ 250 MeV and $1/\Lambda_X > 4 \times 10^{-6}$ GeV^{-1}. Moreover, we see that LUXE phase-1 is expected to probe 40 MeV $\lesssim m_X \lesssim$ 350 MeV and $1/\Lambda_X > 2 \times 10^{-6}$ GeV^{-1}. The region of natural parameter space for scalar is below the brown dashed-dotted line of Fig. 5, which will be probed in phase-1. The projections from the FASER2 (planned for a HL-LHC future run scheduled to start in 2029 [68]) and NA62 in dump mode are roughly similar with the LUXE phase-1 sensitivity curve, that is expected to be reached after one year of running. Finally, We also consider an optimized dump setup with $L_D = 0.5m$ and show the projected sensitivity for illustration.

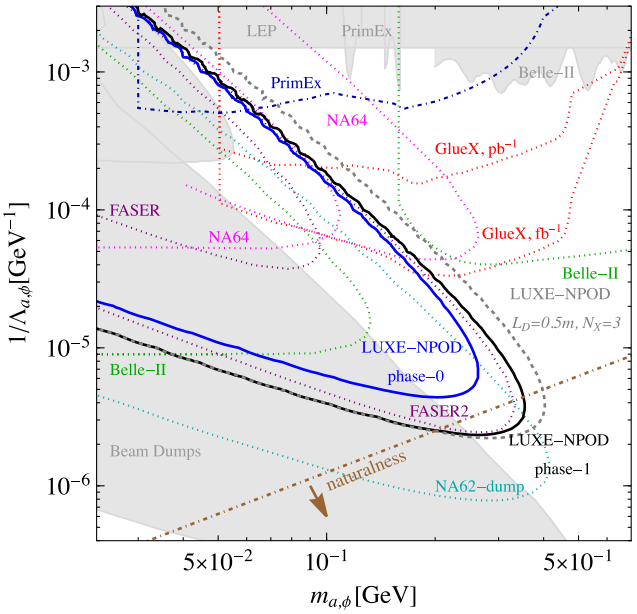

FIG. 5. The projected reach of LUXE-NPOD phase-0 (1) in a solid blue (black) compared to the currently existing bounds (gray regions) on $X = a, \phi$-photon couplings from LEP [54–56], PRIMEX [35], Belle-II [60], NA64 [58,59] and beam-dumps [61,62,69]. The dark blue dot-dashed is the projection from on-tape PRIMEX dataset [35]. The dotted lines are future projections of NA62 (assuming 0 backgrounds), NA64, Belle-II, FASER, PRIMEX and GLUEX [32,35,63–67]. The natural region for the scalar model is below the brown dashed-dotted line. The gray dashed line indicates the LUXE-NPOD phase-1 projection with $L_D = 0.5$ m and background free search.

We comment that in an hypothetical e-dump case, the signal yield will be larger by a factor of few. However, for same dump and detector, the number of background events will be $\gtrsim$150, compared to $\lesssim$1 for LUXE-NPOD). Thus, we conclude that LUXE-NPOD can be background free and a much clean experiment than ordinary e beam dump.

VII. OUTLOOK

The proposed LUXE-NPOD setup provides a novel way of searching for new feebly interacting particles coupling to photons. It has significant advantages compared to using photons produced via bremsstrahlung or electrons or protons on a dump. While in the bremsstrahlung case the NP production will be significantly lower per primary electron, the case of the electron- or proton-beam dump will experience background larger. With a reasonable choice of a detector technology, this search can be regarded as background-free. In this case we show that for the same detector assumption, the background yield in the electrons-on-dump case (and moreover in the protons case) will be larger by at least two orders of magnitudes. An unexplored region of the parameter space can be accessed with just a few days of data taking at a laser repetition rate of 1 Hz. With one year of data taking, this search has the potential to

discover such particles in a unique region of the parameter space.

There are several future directions following this proposal. The first is to investigate spin-0 particles that couple to gluons [35] and types of nonlinear photon dynamics [70–74]. Furthermore there are several experiments that aim to probe strong field QED which can adopt the NPOD concept. In that context, investigating other types of interactions or maybe even changing the flavor of the incoming particles would be also be extremely interesting. Furthermore, it would be interesting to explore what reach could be obtained when using parasitically the high-energy electron beams of future Higgs factories, e.g., the ILC [75], FCC-ee [76], CEPC [77] and CLIC [78]. Finally, high-intensity lasers are rapidly being further improved and a 1 kHz repetition rate should be achievable for 100 TW lasers within the next decade, increasing the photon yield by a factor of 1000 compared to the current proposal, potentially resulting in a large sensitivity gain.

ACKNOWLEDGMENTS

The authors would like to thank Or Hen, Ben King, Andreas Ringwald, Mike Williams for useful discussions, Iftah Galon for help with MADGRAPH5. We are also grateful to Ben King, Federico Meloni, and Mike Williams for comments on the manuscript. Z. B. thanks the Weizmann Institute of Science for hospitality via the Yutchun Program during the initial phase of this project. O. B. and B. H. thank the DESY directorate for funding this work through the DESY Strategy Fund. The work by B. H. and was in part funded by the Deutsche Forschungsgemeinschaft under Germany's Excellence Strategy—EXC 2121 "Quantum Universe"390833306. T. M. is supported by "Study in Israel" Fellowship for Outstanding Post-Doctoral Researchers from China and India by PBC of CHE. The work of G. P. is supported by grants from BSF-NSF (No. 2019760), Friedrich Wilhelm Bessel research award, GIF, the ISF (Grant No. 718/18), Minerva, SABRA—Yeda-Sela—WRC Program, the Estate of Emile Mimran, and The Maurice and Vivienne Wohl Endowment. The work of Y. S. and T. M. is supported by grants from the NSF-BSF (No. 2018683), by the ISF (Grant No. 482/20) and by the Azrieli foundation. Y. S. is Taub fellow (supported by the Taub Family Foundation). The work of N. T. H. is supported by a research grant from the Estate of Dr. Moshe Glück, the Minerva foundation with funding from the Federal German Ministry for Education and Research, the ISF (Grant No. 708/20), the Anna and Maurice Boukstein Career Development Chair and the Estate of Emile Mimran. Simulations of photon production were enabled by resources provided by the Swedish National Infrastructure for Computing (SNIC) at the High Performance Computing Centre North (HPC2N), partially funded by the Swedish Research Council through Grant agreement No. 2018-05973.

APPENDIX A: SECONDARY NEW PHYSICS PRODUCTION OF SPIN-0 PARTICLES

Contours of the expected number of spin-0 signal events in secondary production are showed in Figs. 6 and 7. The signal estimation is described in the main text by using Eq. (2) and was verified by a MADGRAPH5 simulation.

We comment that a data-driven signal normalization can be achieved by a short run on a thin target (measuring the π^0 and η yields, e.g., [35]).

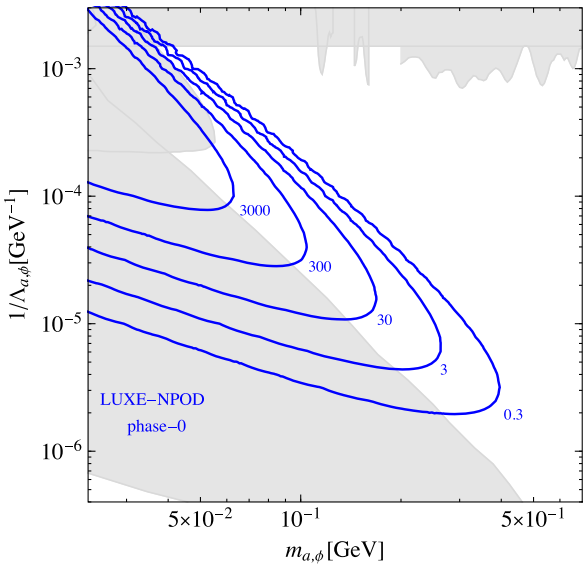

FIG. 6. Contours of the expected number of X events, N_X, for phase-0 compared to the currently existing bounds (gray regions). For further details see Fig. 5.

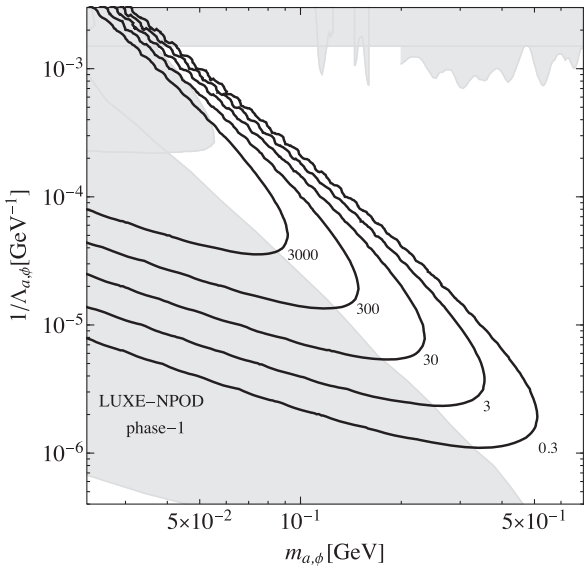

FIG. 7. Contours of the expected number of X events, N_X, for phase-1 compared to the currently existing bounds (gray regions). For further details see Fig. 5.

APPENDIX B: PRIMARY NEW PHYSICS PRODUCTION

In this section we explore primary new physics production, see Fig. 8. In addition to X coupling with photons we explore the ALP/scalar electron coupling, which is captured by

$$\mathcal{L}_{e,a,\phi} = ig_{ae}a\bar{e}\gamma^5 e + g_{\phi e}\phi\bar{e}e. \tag{B1}$$

We also consider "millicharged" particles (mCP) [79–82], denoted here as ψ, with a mass $m_\psi \ll m_e$ and a fractional electric charge $q \ll 1$. The effective mCP-photon interaction can be simply written as

$$\mathcal{L}_\psi = eq\bar{\psi}\not{A}\psi. \tag{B2}$$

Next, we calculate new physics primary production of the processes

$$\begin{aligned} e_{\rm V}^- &\to e_{\rm V}^- + X, \\ e_{\rm V}^- &\to e_{\rm V}^- + \gamma^* \to e_{\rm V}^- + X + \gamma, \\ \gamma\,(\text{or}\,\gamma^*) &\to \psi^+ + \psi^-, \end{aligned} \tag{B3}$$

for relevant works see Refs. [83–87]. The Feynman diagrams of the above processes are plotted in Fig. 9. The ratio between the above production rates and the QED-only Compton scattering for $\xi = 3.4$ and $\chi = 0.65$ are plotted in Fig. 10, where we set $g_{ae} = 10^{-8}$, $\Lambda_a = \text{TeV}$, and $q = 5 \times 10^{-5}$. Our calculation below are based on Ref. [5].

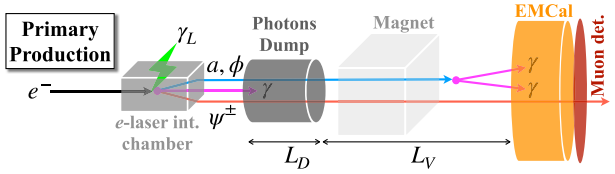

FIG. 8. A schematic illustration of the LUXE-NPOD concept for the primary production mechanism realization in the experimental setup.

1. Nonperturbative X production in a circularly polarized laser

We calculate the nonperturbative Compton emission of ALP and scalar in a circular polarized laser. The background laser field can be written as

$$A_\mu = a_{1\mu}\cos(k\cdot x) + a_{2\mu}\sin(k\cdot x), \tag{B4}$$

where k_μ is the laser four vector, x_μ is the spatial coordinate, $A^2 \equiv a_1^2 = a_2^2$ and $k \cdot a_{1,2} = 0$. The solution of the Dirac equation for electron with momentum p_μ ($p^2 = m_e^2$) in the above laser background is given by the Volkov state [16]

$$\begin{aligned} \psi_{pr}(x) &= \left(1 + \frac{e\not{k}\not{A}}{2kp}\right)u_r(p) \\ &\quad \times \exp\left[-ipx - i\int_0^{kx} d\phi e\left(\frac{pA}{kp} - \frac{eA^2}{2kp}\right)\right] \end{aligned} \tag{B5}$$

$$\begin{aligned} &= \left[1 + \frac{e\not{k}\not{a}_1}{2kp}\sin(kx) + \frac{e\not{k}\not{a}_2}{2kp}\cos(kx)\right]u_r(p) \\ &\quad \times \exp\left[-iqx - ie\left(\frac{a_1 p}{kp}\sin(kx) + \frac{a_2 p}{kp}\cos(kx)\right)\right], \end{aligned} \tag{B6}$$

where $u_r(p)$ is the Dirac spinor in free space. For convenience, we define the followings

$$\begin{aligned} q_\mu &\equiv p_\mu + \frac{e^2a^2}{2(kp)}k_\mu, \qquad \xi = \frac{ea}{m_e}, \\ \chi &\equiv \frac{kq}{m_e^2}\xi = \frac{kp}{m_e^2}\xi, \qquad u \equiv \frac{k\cdot p_a}{k\cdot q'}, \qquad r_m \equiv \frac{m_a}{m_e}, \end{aligned} \tag{B7}$$

such that $m_*^2 \equiv q^2 = m_e^2(1+\xi^2)$.

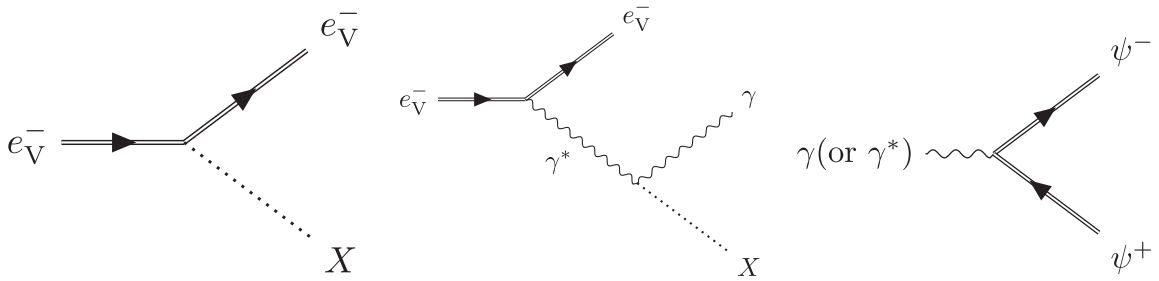

FIG. 9. The Feynman diagrams for primary new physics production, see Eq. (B3). The dressed electron is represented as a double line. Left: $e_{\rm V}^- \to e_{\rm V}^- + X$; middle: $e_{\rm V}^- \to e_{\rm V}^- + \gamma^* \to e_{\rm V}^- + X + \gamma$; right: $\gamma\,(\text{or}\,\gamma^*) \to \psi^+ + \psi^-$.

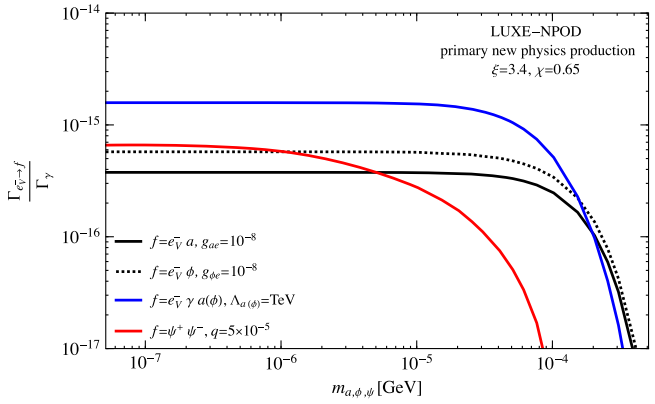

FIG. 10. The new physics primary production rates of processes in Eq. (B3) for $\xi = 3.4$ and $\chi = 0.65$ normalized to the photon production rate, $\tau_\gamma = 1/\Gamma_\gamma \approx 12$ fs.

The $e_V^-(p) \to e_V^-(p')a(p_a)$ amplitude can be written as

$$\mathcal{M}_{e\to ea} = g_{ae}\int \frac{\mathrm{d}^4x}{\sqrt{2^3 p_{a,0}q_0q_0'}}\bar{u}_{r'}(p')\left[\gamma_5 + \frac{4\beta}{ea^2}\not{k}\not{a}_1\gamma_5\sin(kx) + \frac{4\beta}{ea^2}\not{k}\not{a}_2\gamma_5\cos(kx)\right] \times u_r(p)e^{-i(\alpha_1\sin kx-\alpha_2\cos kx)+i(q-q'-p_a)x}, \tag{B8}$$

where

$$\alpha_{1,2} = -e\frac{a_{1,2}\cdot p'}{k\cdot p'}$$
$$\beta = \frac{e^2a^2}{8}\left(\frac{1}{k\cdot q}-\frac{1}{k\cdot q'}\right) = -\frac{u\xi^3}{8\chi_e} \tag{B9}$$

The exponent can be expanded into a Bessel functions as

$$(1,\cos\phi,\sin\phi)e^{-iz\,\sin(\phi-\phi_0)} = \sum_{s=-\infty}^{\infty}(B_1,B_2,B_3)e^{-is\phi}. \tag{B10}$$

with

$$B_1 = J_s(z)e^{-is\phi_0},$$
$$B_2 = \frac{1}{2}[J_{s-1}(z)e^{-i\phi_0} + J_{s+1}e^{i\phi_0}]e^{is\phi_0},$$
$$B_3 = \frac{1}{2i}[J_{s-1}(z)e^{-i\phi_0} - J_{s+1}e^{i\phi_0}]e^{is\phi_0}, \tag{B11}$$

and $z = \sqrt{\alpha_1^2+\alpha_2^2}$ and $\tan\phi_0 = -\alpha_1/\alpha_2$. The ALP emission rate is evaluated by squaring the amplitude and evaluating the phase space integration, which is straightforward in the center of mass system. The resulting rate is

$$\Gamma_{e\to ea} = -\frac{g_{ae}^2m_e^2}{8\pi q^0}\sum_{s>s_0}\int_{u_1}^{u_2}\frac{\mathrm{d}u}{(1+u)^2} \times\left\{\left[\frac{r_m^2}{2}+\xi^2\left(\frac{1+(1+u^2)}{2(1+u)}-\frac{s\chi}{\xi^3(1+u)}-1\right)\right]J_s^2(z) - \frac{\xi^2}{4}\frac{u}{1+u}[J_{s-1}^2(z)+J_{s+1}^2(z)]\right\}, \tag{B12}$$

where

$$z = \frac{\xi^2}{\chi}\sqrt{\left(\frac{2s\chi}{\xi}-r_m^2\right)u-(1+\xi^2)u^2-r_m^2}, \tag{B13}$$

$$s_0 = \frac{r_m\xi}{\chi_e}(r_m+2\sqrt{1+\xi^2}), \tag{B14}$$

$$u_{1,2} = \frac{s\chi}{\xi(1+\xi^2)}-\frac{r_m^2}{2(1+\xi^2)} \pm\sqrt{\left(\frac{s\chi}{\xi(1+\xi^2)}-\frac{r_m^2}{2(1+\xi^2)}\right)^2-\frac{r_m^2}{1+\xi^2}}. \tag{B15}$$

The production rate of scalar with electron coupling is $g_{\phi e}\phi\bar{e}e$ via the process of $e_V^- \to e_V^- + \phi$ is calculated similar to the case of ALP. The rate is given by

$$\Gamma_{e\to e\phi} = \frac{g_{\phi e}^2m_e^2}{8\pi q^0}\sum_{s>s_0}\int_{u_1}^{u_2}\frac{\mathrm{d}u}{(1+u)^2} \times\left\{\left[2-\frac{r_m^2}{2}-\xi^2\left(\frac{1+(1+u^2)}{2(1+u)}-\frac{s\chi}{\xi^3(1+u)}-1\right)\right]J_s^2(z) + \frac{\xi^2}{4}\frac{u}{1+u}[J_{s-1}^2(z)+J_{s+1}^2(z)]\right\}, \tag{B16}$$

2. Off-shell ALP production in a circularly polarized laser

The amplitude for the process $e_V^-(p) \to e_V^-(p') + \gamma(k') + a(p_a)$ or $e_V^-(p) \to e_V^-(p') + \gamma(k') + \phi(p_\phi)$, can be written as

$$\mathcal{M}_{e\to e\gamma a(\phi)} = \frac{e}{l^2}\sum_s\bar{u}_{r'}(p')\left\{\left[\not{G}+\frac{e^2A^2(k\cdot G)\not{k}}{2(k\cdot p)(k\cdot p')}\right]C_0 + e\left[\frac{\not{a}_1\not{k}\not{G}}{2k\cdot p'}+\frac{\not{G}\not{k}\not{a}_1}{2k\cdot p}\right]C_1 + e\left[\frac{\not{a}_2\not{k}\not{G}}{2k\cdot p'}+\frac{\not{G}\not{k}\not{a}_2}{2k\cdot p}\right]C_2\right\}u_r(p), \tag{B17}$$

where $l = k' + p_a$, $G_\nu = \frac{l^\mu k'_\rho\epsilon^*_\sigma(k')\epsilon^{\mu\nu\rho\sigma}}{\Lambda_a}$ ($G_\nu = \frac{l\cdot k'\epsilon^*_\nu(k')-l\cdot\epsilon^*_\sigma(k')k'_\nu}{\Lambda_\phi}$) parametrizes the ALP-photon (scalar-photon) interaction and

$$C_0(s\alpha_1\alpha_2) = J_s(z)e^{-is\varphi}, \tag{B18}$$

$$C_1(s\alpha_1\alpha_2) = \left[\frac{s}{z}J_s(z)\cos\varphi + iJ_s'(z)\sin\varphi\right]e^{-is\varphi}, \quad \text{(B19)}$$

$$C_2(s\alpha_1\alpha_2) = \left[\frac{s}{z}J_s(z)\sin\varphi - iJ_s'(z)\cos\varphi\right]e^{-is\varphi}, \quad \text{(B20)}$$

with φ is the azimuthal angle of the outgoing electron,

$$\begin{aligned}\alpha_i &= e\left(\frac{a_i\cdot p}{k\cdot p} - \frac{a_i\cdot p'}{k\cdot p'}\right),\\ z &= \sqrt{\alpha_1^2+\alpha_2^2} = \frac{\xi^2}{\chi}\sqrt{(1+u)(\lambda_2-\lambda)},\\ \cos\varphi &= \frac{\alpha_1}{z}\\ J_s'(z) &= \frac{dJ_s(z)}{dz}.\end{aligned} \quad \text{(B21)}$$

The ALP production rate per unit time and unit volume can be obtained

$$W = \frac{1}{2VT}\sum_{rr'}\int\frac{d^3p_a d^3k' d^3q'}{(2\pi)^9(2E_a)(2E_\gamma)(2q_0')}|\mathcal{M}_{e\to e\gamma a(\phi)}|^2(2\pi)^4 \times\delta^{(4)}(sk+q-q'-l). \quad \text{(B22)}$$

We integrate over the ALP and photon phase space and express the outgoing electron phase space integration d^3q' in terms of new variables $u = k\cdot l/k\cdot q'$ and $\lambda = l^2/m_e^2$. Therefore, we get that the ALP off-shell production rate per initial electron per unit volume is.

$$\begin{aligned}\Gamma_{e\to e\gamma a(\phi)} &= \frac{2\pi\alpha m_e^2}{q_0\Lambda_{a(\phi)}^2}\sum_{s>s_0}\int\frac{d^3q'}{q_0'}w\\ &= \frac{2\pi^2\alpha m_e^4}{q_0\Lambda^2}\sum_{s>s_0}\int_{u_1}^{u_2}\frac{du}{(1+u)^2}\int_{\lambda_1}^{\lambda_2}d\lambda w,\end{aligned} \quad \text{(B23)}$$

where

$$\begin{aligned}w = &\frac{4(s^2J_s^2+z^2J_s'^2)\lambda\xi^4(u^2+2u+2)-4z^2J_s^2X}{\lambda^2\xi^2(u+1)z^2}\\ &\times\frac{(\lambda-\lambda_1)^3}{3072\pi^4\lambda^2},\end{aligned} \quad \text{(B24)}$$

$$\begin{aligned}X = &\lambda^2\xi^2(u+1) - 8s^2\chi_e^2\\ &+\lambda\xi(\xi^3(u^2+2u+2)+2\xi(u+1)-4su\chi_e),\end{aligned} \quad \text{(B25)}$$

$$s_0 = \frac{(m_a+m_e^*)^2-m_e^{*2}}{2k\cdot q} = \frac{r_m\xi}{2\chi}(r_m+2\sqrt{1+\xi^2}), \quad \text{(B26)}$$

where the Bessel functions argument is z, $E_s^2 = (q+sk)^2 = m_e^2(\xi^3+\xi+2s\chi_e)/\xi$ and

$$\begin{aligned}u_{2,1} &= \frac{E_s^2-m_a^2-m_e^{*2}\pm\sqrt{(E_s^2-m_a^2-m_e^{*2})^2-4m_a^2m_e^{*2}}}{2m_e^{*2}}\\ &= \frac{2s\xi-r_m^2\xi\pm\sqrt{r_m^4\xi^2+4s^2\chi_e^2-4r_m^2\xi(\xi+\xi^3+s\chi_e)}}{2\xi(1+\xi^2)},\end{aligned} \quad \text{(B27)}$$

$$\lambda_1 = r_m^2, \qquad \lambda_2 = \frac{E_s^2u}{m_e^2(1+u)} - (1+\xi^2)u. \quad \text{(B28)}$$

3. Millicharged particle production in a circularly polarized laser

The direct production of millicharged particle (mCP) pairs by high-energy photons in a strong laser background: see also the right-hand panel of Fig. 9 and Eq. (B3). Here we consider the case where the high-energy photons are produced by nonlinear Compton scattering, i.e., where the photons are emitted and subsequently decay within the same laser pulse. The rate (per unit time) at which mCP pairs are produced by nonlinear Compton photons in an ultraintense electromagnetic (EM) wave with invariant amplitude ξ and wave vector κ, is given by:

$$\Gamma_{\rm mCP} = \frac{1}{\Gamma_\gamma}\int_0^1\Gamma_\pm(s\eta_e,\xi,q,r_m)\frac{d\Gamma_\gamma(\eta_e,\xi)}{ds}ds, \quad \text{(B29)}$$

where $\Gamma_\pm(\eta_\gamma,\xi,q,r_m)$ is the rate at which a photon with energy parameter $\eta_\gamma = \kappa\cdot k/m_e^2$ (momentum k) creates a pair of particles with charge and mass ratio q and $r_m = m_\psi/m_e$, $\Gamma_\gamma(\eta_e,\xi)$ is the rate at which an electron with energy parameter $\eta_e = \kappa\cdot p/m_e^2$ (momentum p) emits photons, and $s = \eta_\gamma/\eta_e$. (The quantum parameter is recovered as $\chi_e = \xi\eta_e$.)

We use the rates as calculated in the locally monochromatic approximation [44,45], which assumes the background EM field is a plane wave. For the photon emission rate, we have

$$\begin{aligned}\frac{d\Gamma_\gamma(\eta_e,\xi)}{ds} = -\frac{\alpha m^2}{p^0}\sum_{n=1}^{\infty}\Bigg\{&J_n^2(z)+\frac{\xi^2}{2}\left[1+\frac{s^2}{2(1-s)}\right]\\ &\times[2J_n^2(z)-J_{n-1}^2(z)-J_{n+1}^2(z)]\Bigg\},\end{aligned} \quad \text{(B30)}$$

where the bounds on s, for each n, are $0 < s < s_n/(1+s_n)$, and the auxiliary variables are

$$z^2 = \frac{4n^2\xi^2}{1+\xi^2}\frac{s}{s_n(1-s)}\left[1-\frac{s}{s_n(1-s)}\right], \qquad s_n = \frac{2n\eta_e}{1+\xi^2}. \quad \text{(B31)}$$

For the mCP pair creation rate, we have

$$\frac{d\Gamma_{\pm}(\eta_\gamma,\xi,q,r_m)}{ds} = q^2 r_m^2 \frac{\alpha m^2}{k^0}\sum_{n=n_\star}^{\infty}\left\{J_n^2(z) - \frac{\xi^2}{2}\left[\frac{1}{2s(1-s)}-1\right] \times [2J_n^2(z) - J_{n-1}^2(z) - J_{n+1}^2(z)]\right\}, \tag{B32}$$

where $n_\star = \lceil 2r_m^2(1+q^2\xi^2/r_m^2)/\eta_\gamma\rceil$, $\frac{1}{2}[1-(1-4/s_n)^{1/2}] < s < \frac{1}{2}[1-(1-4/s_n)^{1/2}]$, and the auxiliary variables are

$$z^2 = \frac{4n^2q^2\xi^2/r_m^2}{1+q^2\xi^2/r_m^2}\frac{1}{s_n s(1-s)}\left[1-\frac{1}{s_n s(1-s)}\right],$$
$$s_n = \frac{2n\eta_\gamma/r_m^2}{1+q^2\xi^2/r_m^2}. \tag{B33}$$

Equations (B32) and (B33) are obtained from the electron-positron pair creation rates by making the following transformations: $\alpha \to q^2\alpha$, $m_e \to r_m m_e$, $\xi \to q\xi/r_m$, and $\eta \to \eta/r_m^2$. The result of the calculation is $\Gamma_{\rm mCP}$ as a function of ξ and η_e, for given charge and mass fraction q and r_m.

APPENDIX C: THE CORRELATION BETWEEN PHOTONS AND NEUTRONS BACKGROUNDS

Figure 11 shows the energy distributions (top) and production vertex's z coordinate (bottom) of photons and neutrons. The data shown in the figure is taken from a full GEANT4 v 10.06.p01 [46–48] simulation (using the QGSP_BERT physics list) of two bunch crossings for the nominal LUXE-NPOD setup. Altogether there are 10^{10} primary photons distributed in energy as in Fig. 2 (for phase-1). These primary photons are shot on the dump and produce electromagnetic and hadronic showers of particles, which may escape the dump volume. The kinematic properties of all particles which escape the dump and arrive at the detector face are saved for further analysis. Since the $E > 0.5$ GeV requirement leaves zero photons and only a handful of neutrons for $L_D = 1$ m, this requirement is relaxed in order to plot the distributions seen in Fig. 11. It can be seen in the top plot that the energy of most of the particles is well below the photon's minimum energy of 0.5 GeV used in this work. The correlation between the production of photons to that of neutrons cannot be trivially explained within the scope of this work, but it can be clearly seen in the bottom plot. This correlation is seen also in Fig. 4. It can be expected that the correlation in the production is independent of the particles minimum energy, as long as one looks at samples obtained using the same minimum energy for the two species (photons and neutrons). While the dump is modeled as a 1 m-long cylinder (stretching from $z = 500$ mm to $z = 1500$ mm), the concrete support structure length is 0.5 m (stretching from $z = 750$ mm to $z = 1250$ mm) with a matching cylindrical slot, where the dump lies upon. Therefore, the spectra continuity is altered at these two special points and the increase in the spectra at these two points is essentially due to particles leaking out of the dump and scattering off the concrete support to reach the detector. The particles coming from the concrete support usually arrive very late to the detector face, typically more than 1 μs later than the prompt photons we expect from the signal and they are usually softer than the particles coming from the dump end itself.

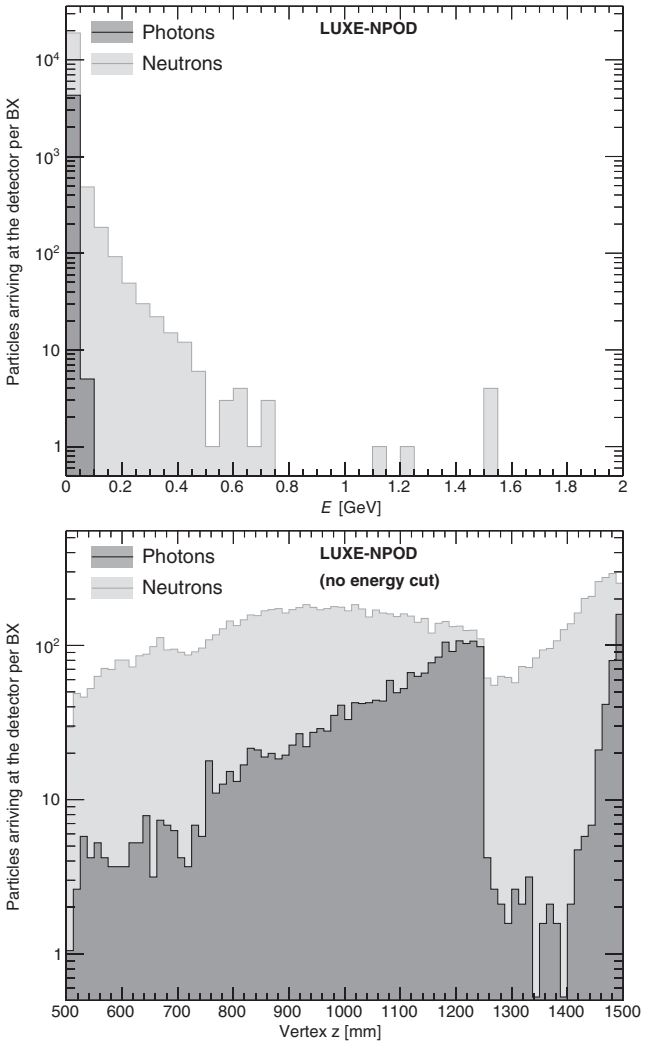

FIG. 11. The energy (top) and the production vertex z-coordinate (bottom) of all background neutrons and photons arriving at the detector face for the LUXE-NPOD setup. The two distributions are given with no energy cut. The production vertex distribution is only shown for the range of the 1 m long dump. The structures seen in the vertex distribution ($z = 750$ mm and $z = 1250$ mm) are due to the shorter (0.5 m) dump's supporting structure (made of concrete). The data in the two distributions correspond to two fully simulated bunch crossings.

APPENDIX D: SEPARATION OF PHOTONS AT THE DETECTOR

We argue that the two signal photons can be efficiently separated, based on current EM calorimeters, even for the case of $m_X \lesssim 100$ MeV, where the two photons may be highly collimated. Sampling EM calorimeters provide measurements of the energy distribution in transverse plane as a function of depth. Having detailed transverse shower shape at different depth allows to improve position, and showers resolutions, and does not limit them by the Moliere radius. In addition, with a compact design, the Moliere radius can reach that of the absorber (W), ∼11 mm [88] and effective Moliere radius evaluated using several initial layers can be as small as ∼8 mm, see Ref. [89]. Reference [53] combines calorimeter with high resolution tracking layers embedded at different depth. Therefore, achieving the required resolution is challenging, but possible considering present developments in calorimeter technologies.

Moreover, in our detailed MADGRAPH5 simulation we check what is the number of signal events, where the spatial separation between the two signal photons of one X decay at the surface of the detector (denoted as Δr) is smaller than 20, 40, and 50 mm for several masses and decay constants close to the edge of our reach. This is summarized in Table II below and Fig. 12.

TABLE II. The fraction (in %) of signal events lost due to different minimum spatial separations between the two photons, Δr, in the calorimeter for different signal scenarios.

m_X [MeV]	Λ_X [GeV^{-1}]	$\Delta r < 20$ mm [%]	$\Delta r < 40$ mm [%]	$\Delta r < 50$ mm [%]
50	10^{-4}	13	30	38
100	10^{-5}	8.4	17	22
150	6×10^{-6}	5.2	11	13
200	4×10^{-6}	3.8	7.6	9.7

As we can see, the typical effect on the signal efficiency is less than 40% and in most cases much smaller. Thus, we can conclude that the effect on our projections is small. A more detailed study is strongly depending on the specific design of the detector and it is beyond the scope of our current paper.

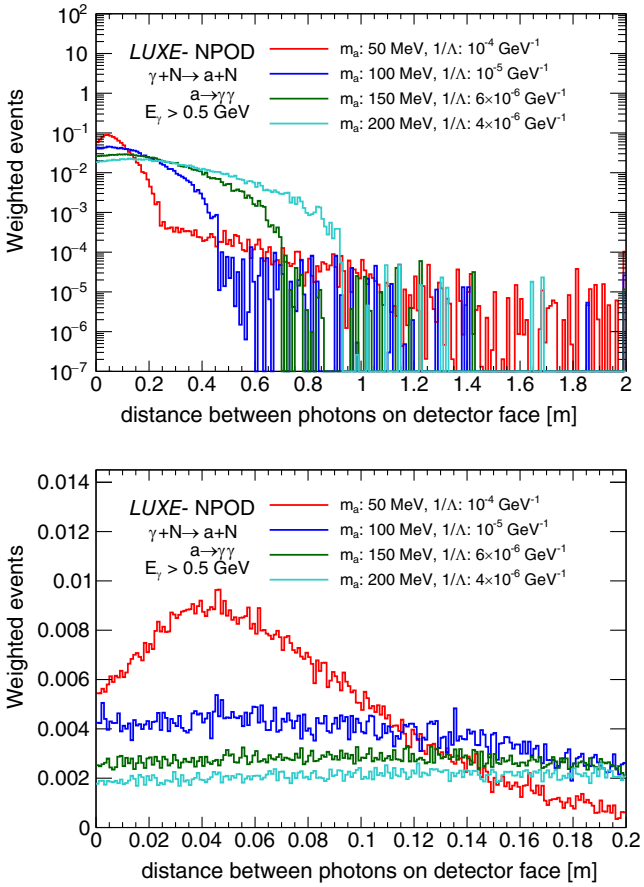

FIG. 12. The spatial distance, d at the detector surface between the two photons ($X \to \gamma\gamma$) for different X models. The top plot is a zoomed in version ($d < 20$ cm) of the bottom plot.

[1] R. K. Ellis *et al.*, Physics briefing book: Input for the European strategy for particle physics update 2020, arXiv: 1910.11775.

[2] F. Sauter, Uber das Verhalten eines Elektrons im homogenen elektrischen Feld nach der relativistischen Theorie Diracs, Z. Phys. **69**, 742 (1931).

[3] W. Heisenberg and H. Euler, Consequences of Dirac's theory of positrons, Z. Phys. **98**, 714 (1936).

[4] J. S. Schwinger, On gauge invariance and vacuum polarization, Phys. Rev. **82**, 664 (1951).

[5] V. I. Ritus, Quantum effects of the interaction of elementary particles with an intense electromagnetic field, J. Sov. Laser Res. **6**, 497 (1985).

[6] A. Di Piazza, C. Muller, K. Z. Hatsagortsyan, and C. H. Keitel, Extremely high-intensity laser interactions with fundamental quantum systems, Rev. Mod. Phys. **84**, 1177 (2012).

[7] A. G. R. Thomas, C. P. Ridgers, S. S. Bulanov, B. J. Griffin, and S. P. D. Mangles, Strong Radiation-Damping Effects in a Gamma-Ray Source Generated by the Interaction of a

High-Intensity Laser with a Wakefield-Accelerated Electron Beam, Phys. Rev. X **2**, 041004 (2012).
[8] W. Yan, C. Fruhling, G. Golovin, D. Haden, J. Luo, P. Zhang, B. Zhao, J. Zhang, C. Liu, M. Chen, S. Chen, S. Banerjee, and D. Umstadter, High-order multiphoton Thomson scattering, Nat. Photonics **11**, 514 (2017).
[9] J. Magnusson, A. Gonoskov, M. Marklund, T. Z. Esirkepov, J. K. Koga, K. Kondo, M. Kando, S. V. Bulanov, G. Korn, and S. S. Bulanov, Laser-Particle Collider for Multi-GeV Photon Production, Phys. Rev. Lett. **122**, 254801 (2019).
[10] H. Abramowicz *et al.*, Letter of Intent for the LUXE Experiment, arXiv:1909.00860.
[11] H. Abramowicz *et al.*, Conceptual design report for the LUXE experiment, Eur. Phys. J. Special Topics **230**, 2445 (2021).
[12] M. Altarelli *et al.*, XFEL: The European x-ray free-electron laser, Technical Design Report No. DESY-06-097, 2006, 10.3204/DESY_06-097.
[13] A. HartinEnhanced, high energy photon production from resonant Compton scattering in a strong external field, Nucl. Instrum. Methods Phys. Res., Sect. B **402**, 339 (2017).
[14] A. Gonoskov, T. G. Blackburn, M. Marklund, and S. S. Bulanov, Charged particle motion and radiation in strong electromagnetic fields, Rev. Mod. Phys. **94**, 045001 (2022).
[15] A. Fedotov, A. Ilderton, F. Karbstein, B. King, D. Seipt, H. Taya, and G. Torgrimsson, Advances in QED with intense background fields, arXiv:2203.00019.
[16] D. M. Wolkow, Uber eine Klasse von Losungen der Diracschen Gleichung, Z. Phys. **94**, 250 (1935).
[17] W. H. Furry, On bound states and scattering in positron theory, Phys. Rev. **81**, 115 (1951).
[18] A. I. Nikishov and V. I. Ritus, Quantum processes in the field of a plane electromagnetic wave and in a constant field 1, Sov. Phys. JETP **19**, 529 (1964).
[19] L. S. Brown and T. W. B. Kibble, Interaction of intense laser beams with electrons, Phys. Rev. **133**, A705 (1964).
[20] H. R. Reiss, Absorption of light by light, J. Math. Phys. (N.Y.) **3**, 59 (1962).
[21] P. A. Zyla *et al.* (Particle Data Group), Review of particle physics, Prog. Theor. Exp. Phys. **2020**, 083C01 (2020).
[22] D. J. E. Marsh, Axion cosmology, Phys. Rep. **643**, 1 (2016).
[23] P. W. Graham, I. G. Irastorza, S. K. Lamoreaux, A. Lindner, and K. A. van Bibber, Experimental searches for the axion and axion-like particles, Annu. Rev. Nucl. Part. Sci. **65**, 485 (2015).
[24] A. Hook, TASI lectures on the strong *CP* problem and axions, Proc. Sci. TASI2018 (**2019**) 004 [arXiv:1812.02669].
[25] I. G. Irastorza and J. Redondo, New experimental approaches in the search for axion-like particles, Prog. Part. Nucl. Phys. **102**, 89 (2018).
[26] K. Choi, S. H. Im, and C. S. Shin, Recent progress in physics of axions or axion-like particles, Annu. Rev. Nucl. Part. Sci. **71**, 225 (2021).
[27] W. D. Goldberger, B. Grinstein, and W. Skiba, Distinguishing the Higgs Boson from the Dilaton at the Large Hadron Collider, Phys. Rev. Lett. **100**, 111802 (2008).
[28] T. Flacke, C. Frugiuele, E. Fuchs, R. S. Gupta, and G. Perez, Phenomenology of relaxion-Higgs mixing, J. High Energy Phys. 06 (2017) 050.
[29] K. Choi and S. H. Im, Constraints on relaxion windows, J. High Energy Phys. 12 (**2016**) 093.
[30] P. W. Graham, D. E. Kaplan, and S. Rajendran, Cosmological Relaxation of the Electroweak Scale, Phys. Rev. Lett. **115**, 221801 (2015).
[31] A. Banerjee, H. Kim, O. Matsedonskyi, G. Perez, and M. S. Safronova, Probing the relaxed relaxion at the luminosity and precision frontiers, J. High Energy Phys. 07 (2020) 153.
[32] A. Berlin, S. Gori, P. Schuster, and N. Toro, Dark sectors at the Fermilab SeaQuest experiment, Phys. Rev. D **98**, 035011 (2018).
[33] C.-Y. Chen, M. Pospelov, and Y.-M. Zhong, Muon beam experiments to probe the dark sector, Phys. Rev. D **95**, 115005 (2017).
[34] Y.-S. Tsai, Axion bremsstrahlung by an electron beam, Phys. Rev. D **34**, 1326 (1986).
[35] D. Aloni, C. Fanelli, Y. Soreq, and M. Williams, Photoproduction of Axionlike Particles, Phys. Rev. Lett. **123**, 071801 (2019).
[36] T. Stelzer and W. F. Long, Automatic generation of tree level helicity amplitudes, Comput. Phys. Commun. **81**, 357 (1994).
[37] J. Alwall, M. Herquet, F. Maltoni, O. Mattelaer, and T. Stelzer, MADGRAPH5: Going beyond, J. High Energy Phys. 06 (2011) 128.
[38] J. Alwall, R. Frederix, S. Frixione, V. Hirschi, F. Maltoni, O. Mattelaer, H. S. Shao, T. Stelzer, P. Torrielli, and M. Zaro, The automated computation of tree-level and next-to-leading order differential cross sections, and their matching to parton shower simulations, J. High Energy Phys. 07 (2014) 079.
[39] C. Degrande, C. Duhr, B. Fuks, D. Grellscheid, O. Mattelaer, and T. Reiter, UFO—The universal FeynRules output, Comput. Phys. Commun. **183**, 1201 (2012).
[40] I. Brivio, M. B. Gavela, L. Merlo, K. Mimasu, J. M. No, R. del Rey, and V. Sanz, ALPs effective field theory and collider signatures, Eur. Phys. J. C **77**, 572 (2017).
[41] Y.-S. Tsai, Pair production and bremsstrahlung of charged leptons, Rev. Mod. Phys. **46**, 815 (1974); **49**, 421(E) (1977).
[42] J. D. Bjorken, R. Essig, P. Schuster, and N. Toro, New fixed-target experiments to search for dark gauge forces, Phys. Rev. D **80**, 075018 (2009).
[43] T. G. Blackburn, https://github.com/tgblackburn/ptarmigan.
[44] T. Heinzl, B. King, and A. J. Macleod, The locally monochromatic approximation to QED in intense laser fields, Phys. Rev. A **102**, 063110 (2020).
[45] T. G. Blackburn, A. J. MacLeod, and B. King, From local to nonlocal: Higher fidelity simulations of photon emission in intense laser pulses, New J. Phys. **23**, 085008 (2021).
[46] S. Agostinelli *et al.* (GEANT4 Collaboration), GEANT4–a simulation toolkit, Nucl. Instrum. Methods Phys. Res., Sect. A **506**, 250 (2003).
[47] J. Allison *et al.*, GEANT4 developments and applications, IEEE Trans. Nucl. Sci. **53**, 270 (2006).
[48] J. Allison *et al.*, Recent developments in GEANT4, Nucl. Instrum. Methods Phys. Res., Sect. A **835**, 186 (2016).
[49] A. Bornheim, Timing performance of the CMS electromagnetic calorimeter and prospects for the future, Proc. Sci. TIPP2014 (**2015**) 021.

[50] A. Lobanov, Precision timing calorimetry with the CMS HGCAL, J. Instrum. **15**, C07003 (2020).

[51] L. Martinazzoli, Crystal fibers for the LHCb calorimeter upgrade, IEEE Trans. Nucl. Sci. **67**, 1003 (2020).

[52] Y. Liu, J. Jiang, and Y. Wang, High-granularity crystal calorimetry: Conceptual designs and first studies, J. Instrum. **15**, C04056 (2020).

[53] W. M. Bonivento, Studies for the electro-magnetic calorimeter SplitCal for the SHiP experiment at CERN with shower direction reconstruction capability, J. Instrum. **13**, C02041 (2018).

[54] J. Jaeckel and M. Spannowsky, Probing MeV to 90 GeV axion-like particles with LEP and LHC, Phys. Lett. B **753**, 482 (2016).

[55] S. Knapen, T. Lin, H. K. Lou, and T. Melia, Searching for Axionlike Particles with Ultraperipheral Heavy-Ion Collisions, Phys. Rev. Lett. **118**, 171801 (2017).

[56] G. Abbiendi *et al.* (OPAL Collaboration), Multiphoton production in e^+e^- collisions at $s**(1/2) = 181$-GeV to 209-GeV, Eur. Phys. J. C **26**, 331 (2003).

[57] I. Larin *et al.* (PrimEx Collaboration), A New Measurement of the π^0 Radiative Decay Width, Phys. Rev. Lett. **106**, 162303 (2011).

[58] R. R. Dusaev, D. V. Kirpichnikov, and M. M. Kirsanov, Photoproduction of axionlike particles in the NA64 experiment, Phys. Rev. D **102**, 055018 (2020).

[59] D. Banerjee *et al.* (NA64 Collaboration), Search for Axionlike and Scalar Particles with the NA64 Experiment, Phys. Rev. Lett. **125**, 081801 (2020).

[60] F. Abudinén *et al.* (Belle-II Collaboration), Search for Axion-Like Particles Produced in e^+e^- Collisions at Belle II, Phys. Rev. Lett. **125**, 161806 (2020).

[61] J. D. Bjorken, S. Ecklund, W. R. Nelson, A. Abashian, C. Church, B. Lu, L. W. Mo, T. A. Nunamaker, and P. Rassmann, Search for neutral metastable penetrating particles produced in the SLAC beam dump, Phys. Rev. D **38**, 3375 (1988).

[62] J. Blumlein *et al.*, Limits on neutral light scalar and pseudoscalar particles in a proton beam dump experiment, Z. Phys. C **51**, 341 (1991).

[63] J. Beacham *et al.*, Physics beyond colliders at CERN: Beyond the Standard Model Working Group Report, J. Phys. G **47**, 010501 (2020).

[64] B. Döbrich, J. Jaeckel, F. Kahlhoefer, A. Ringwald, and K. Schmidt-Hoberg, ALPtraum: ALP production in proton beam dump experiments, J. High Energy Phys. 02 (2016) 018.

[65] B. Döbrich, J. Jaeckel, and T. Spadaro, Light in the beam dump—ALP production from decay photons in proton beam-dumps, J. High Energy Phys. 05 (2019) 213; 10 (2020) 046(E).

[66] M. J. Dolan, T. Ferber, C. Hearty, F. Kahlhoefer, and K. Schmidt-Hoberg, Revised constraints and Belle II sensitivity for visible and invisible axion-like particles, J. High Energy Phys. 12 (2017) 094; 03 (2021) 190(E).

[67] J. L. Feng, I. Galon, F. Kling, and S. Trojanowski, Axionlike particles at FASER: The LHC as a photon beam dump, Phys. Rev. D **98**, 055021 (2018).

[68] G. Apollinari, O. Brüning, T. Nakamoto, and L. Rossi, High luminosity Large Hadron Collider HL-LHC, arXiv: 1705.08830.

[69] J. Blumlein *et al.*, Limits on the mass of light (pseudo)scalar particles from Bethe-Heitler e^+e^- and $\mu^+\mu^-$ pair production in a proton—iron beam dump experiment, Int. J. Mod. Phys. A **07**, 3835 (1992).

[70] D. Bernard, On the potential of light by light scattering for invisible axion detection, Nuovo Cimento Soc. Ital Fis. **110A**, 1339 (1997).

[71] S. Evans and J. Rafelski, Virtual axion-like particle complement to Euler-Heisenberg-Schwinger action, Phys. Lett. B **791**, 331 (2019).

[72] Z. Bogorad, A. Hook, Y. Kahn, and Y. Soreq, Probing Axionlike Particles and the Axiverse with Superconducting Radio-Frequency Cavities, Phys. Rev. Lett. **123**, 021801 (2019).

[73] C. Gao and R. Harnik, Axion searches with two superconducting radio-frequency cavities, J. High Energy Phys. 07 (2021) 053.

[74] M. Gorghetto, G. Perez, I. Savoray, and Y. Soreq, Probing *CP* violation in photon self-interactions with cavities, J. High Energy Phys. 10 (**2021**) 056.

[75] H. Baer *et al.*, The International Linear Collider Technical Design Report—Volume 2: Physics, arXiv:1306.6352.

[76] A. Abada *et al.* (FCC Collaboration), FCC-ee: The Lepton Collider: Future Circular Collider Conceptual Design Report Volume 2, Eur. Phys. J. Special Topics **228**, 261 (2019).

[77] M. Dong *et al.* (CEPC Study Group Collaboration), CEPC Conceptual Design Report: Volume 2—Physics & Detector, arXiv:1811.10545.

[78] L. Linssen, A. Miyamoto, M. Stanitzki, and H. Weerts, Physics and Detectors at CLIC: CLIC Conceptual Design Report, arXiv:1202.5940.

[79] B. Holdom, Two U(1)'s and Epsilon charge shifts, Phys. Lett. **166B**, 196 (1986).

[80] K. R. Dienes, C. F. Kolda, and J. March-Russell, Kinetic mixing and the supersymmetric gauge hierarchy, Nucl. Phys. **B492**, 104 (1997).

[81] S. A. Abel and B. W. Schofield, Brane anti-brane kinetic mixing, millicharged particles and SUSY breaking, Nucl. Phys. **B685**, 150 (2004).

[82] B. Batell and T. Gherghetta, Localized U(1) gauge fields, millicharged particles, and holography, Phys. Rev. D **73**, 045016 (2006).

[83] B. M. Dillon and B. King, Light scalars: Coherent nonlinear Thomson scattering and detection, Phys. Rev. D **99**, 035048 (2019).

[84] B. M. Dillon and B. King, ALP production through nonlinear Compton scattering in intense fields, Eur. Phys. J. C **78**, 775 (2018).

[85] B. King, Electron-seeded ALP production and ALP decay in an oscillating electromagnetic field, Phys. Lett. B **782**, 737 (2018).

[86] B. King, B. M. Dillon, K. A. Beyer, and G. Gregori, Axion-like-particle decay in strong electromagnetic backgrounds, J. High Energy Phys. 12 (2019) 162.

[87] S. Villalba-Chavez and C. Muller, Photo-production of scalar particles in the field of a circularly polarized laser beam, Phys. Lett. B **718**, 992 (2013).

[88] C. Zhang (ALICE FoCal Group Collaboration), FoCal—A high granularity electromagnetic calorimeter for forward direct photon measurements, Nucl. Instrum. Methods Phys. Res., Sect. A **845**, 542 (2017).

[89] H. Abramowicz *et al.*, Performance and Molière radius measurements using a compact prototype of LumiCal in an electron test beam, Eur. Phys. J. C **79**, 579 (2019).